# Relative Accuracy Evaluation of UAV Photogrammetry for Drifting Arctic Sea Ice

Zhiqi He [1], Shuhang Zhang [1,2,*], Daikun Yang [1], Wuming Zhang [1,2]

[1] School of Geospatial Engineering and Science, Sun Yat-sen University, Zhuhai, China - zhangsh52@mail.sysu.edu.cn
[2] Key Laboratory of Comprehensive Observation of Polar Environment (Sun Yat-sen University), Ministry of Education, China

**Keywords:** UAV, Photogrammetry, Accuracy, Sea ice, Arctic.

## Abstract

Unmanned aerial vehicle (UAV) photogrammetry is indispensable for Arctic sea ice research, enabling high-resolution mapping and supporting critical operations. However, drifting sea ice, which is characterized by continuous motion that violates the fundamental ‘static-scene’ assumption, and no ground control points (GCPs), poses challenges to orthomosaic accuracy. This study presents a systematic framework for assessing and improving the relative accuracy of UAV photogrammetry over drifting Arctic sea ice, using 18 shipborne UAV missions conducted during the Following Arctic/Antarctic iCE 2024 expedition. A time-dependent correction method based on synchronized vessel GNSS data, referred to as drift correction, was employed to compensate for drift in the exterior orientation parameters of the UAV imagery. In the absence of GCPs, relative accuracy was evaluated using shipborne constrained and check scale bars. Results show that under raw conditions, with a ground sampling distance (GSD) of 2–5 cm, the orthomosaics achieved a mean root mean square error (RMSE) of 0.304 m. The RMSE showed a strong positive correlation with ice drift speed ($r = 0.71$) and drift distance ($r = 0.79$), while the flight–drift angle showed negligible influence ($r = -0.13$). Drift correction alone reduced the mean RMSE to 0.075 m, achieving error reductions of up to 0.6 m under high-drift conditions. The incorporation of scale bar constraints further enhanced accuracy to a mean RMSE of 0.043 m. These findings validate the effectiveness of drift correction and scale-constraint-based optimization, offering a practical framework for accuracy assessment and mission implementation in dynamic polar environments.

## 1. Introduction

Shipborne UAVs have emerged as a critical tool for Arctic research, providing high-resolution, near-real-time imagery that supports safe icebreaker navigation and underwater operations in harsh environments (Li et al., 2023; Komarov and Buehner, 2021). The resulting orthomosaics and digital surface models (DSMs) reveal fine-scale morphological features and provide a spatial foundation for tasks such as sea ice thickness inversion and energy balance modeling (Muilwijk et al., 2024; Rack et al., 2021). With the increasing frequency of precise small-scale operations, such as submersible deployments and ice-surface robot navigation, the geometric fidelity of these data products has become paramount (Chen et al., 2023; Divine et al., 2016). Consequently, the systematic evaluation of the relative accuracy of UAV photogrammetry over drifting sea ice holds significant scientific and practical value.

Compared to terrestrial photogrammetry, Arctic sea ice observations face harsher conditions. Sea ice drift poses a fundamental challenge to UAV photogrammetry in polar regions. Conventional photogrammetry fundamentally relies on a static-scene assumption, presuming that ground object coordinates remain fixed throughout the image acquisition process. However, the continuous translational drift of sea ice during a UAV sortie directly violates this assumption, causing ground features to act as time-correlated moving targets. As shown in Figure 1, during UAV surveys over drifting sea ice, continuous ice motion causes the actual imaged area to deviate from the planned coverage, resulting in incomplete coverage and variable image overlap. This introduces time-accumulated systematic errors in exterior orientation parameters, leading to geometric inconsistencies in orthomosaics (Kim et al., 2021). Although GNSS-based sea ice drift correction has been applied to improve consistency (Neckel et al., 2023), its quantitative effectiveness and broader applicability remain insufficiently evaluated.

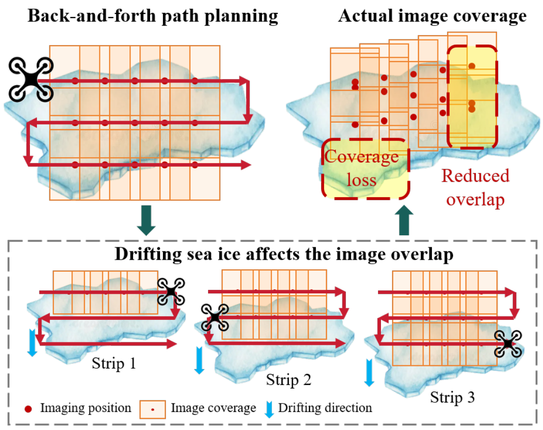


Figure 1. Schematic illustration of the impact of sea ice drift on UAV sea ice observations.

Therefore, quantitatively evaluating the effects of sea ice drift on UAV photogrammetry accuracy remains a key challenge in Arctic environments. Standard GCP-based methods are ineffective in drifting ice due to the absence of fixed benchmarks (Elkhrachy, 2021), necessitating a tailored accuracy assessment framework for mission planning and quality control.

To address these challenges, this study establishes a relative accuracy assessment framework using ship-based constrained and check scale bars. We systematically evaluate orthomosaic quality, quantify the impact of sea ice drift kinematics (speed, distance, and angle), and assess the efficacy of drift correction and scale constraints. The findings offer practical guidelines for future Arctic UAV surveys.

## 2. Data and Method

The overall technical workflow is illustrated in Figure 2. The following sections detail the data and research methods employed in this study.

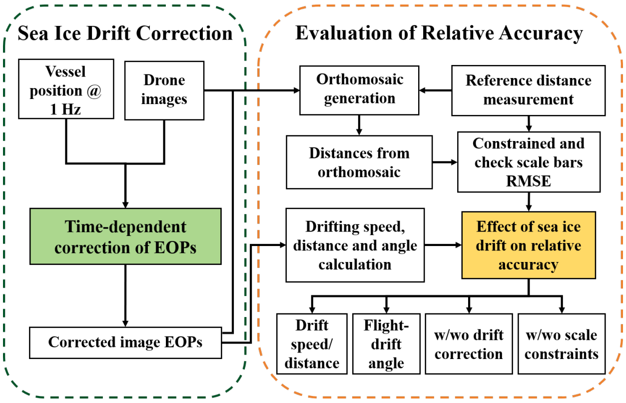


Figure 2. Workflow of the proposed method.

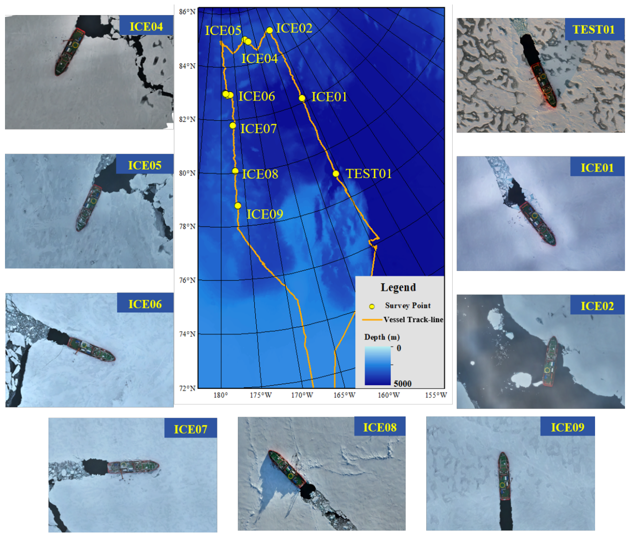


Figure 3. Arctic cruise track of the FACE2024 expedition and distribution of UAV observation locations.

### 2.1 Data Acquisition

**2.1.1 UAV Imagery Acquisition** The UAV-based sea ice imagery utilized in this study was exclusively acquired during the Following Arctic/Antarctic iCE 2024 (FACE2024) expedition. In polar research, an ‘ice station’ refers to a temporary site where the icebreaker moors alongside a drifting ice floe, creating a synchronized platform for in-situ measurements and shipborne UAV surveys. This study utilized 18 sea ice nadir imagery datasets acquired during the FACE2024 expedition. These images were collected by different UAV models at various times from 9 ice stations, with detailed parameters listed in Table 1. Figure 3 illustrates the cruise track, the spatial distribution of ice stations, and detailed views of the study sites for FACE2024 expedition.

**2.1.2 Data Source for Sea Ice Motion** In this study, vessel positioning data recorded during the FACE2024 expedition was also utilized. The vessel positions were logged at a frequency of 1 Hz. When the icebreaker was moored at an ice station, both the vessel and the surrounding sea ice moved synchronously; therefore, the positional variations recorded by the vessel navigation system directly reflected the drift behavior of the underlying sea ice. Consequently, the vessel positioning data accurately capture the kinematic state of the sea ice, providing the essential basis for calculating key motion parameters such as drift speed and drift direction.

### 2.2 Time-Dependent Correction of Exterior Orientation Parameters

This study implemented time-dependent exterior orientation parameters correction strategies (i.e., drift correction) designed to numerically compensate for the ice motion. The drift correction is based on the assumption that the UAV platform and the reference vessel are located on the same drifting ice floe and therefore share an identical translational motion. For each image, three positions are available: the original image position $P_{\text{img}}$ (drift-affected), a fixed reference vessel position $P_{\text{ref}}$ (e.g., the start of the survey), and the synchronized vessel position $P_{\text{gps}}$ at image acquisition. Coordinates are projected to a

| Ice station | Flight ID | Date | UAV model | Number of images | Flight duration (min) | Overlap / side-lap (%) | Flight height (m) | GSD (cm/pix) |
|---|---|---|---|---|---|---|---|---|
| TEST01 | 1 | 2024/08/26 | Feima V500 | 559 | 22 | 80/60 | 190 | 3 |
| ICE01 | 2 | 2024/08/28 | Feima D500 | 812 | 44 | 60/58 | 90 | 2 |
| ICE02 | 3 | 2024/08/30 | DJI M3E | 1071 | 14 | 70/50 | 66 | 2 |
| ICE04 | 4 | 2024/09/01 | DJI M2EA | 220 | 9 | 70/50 | 80 | 3 |
| ICE05 | 5 | 2024/09/01 | DJI M3E | 336 | 8 | 70/50 | 66 | 3 |
| ICE06 | 6 | 2024/09/04 | DJI M3E | 314 | 11 | 70/50 | 96 | 3 |
| | 7 | 2024/09/04 | DJI M3E | 332 | 8 | 70/50 | 66 | 2 |
| | 8 | 2024/09/04 | DJI M3E | 567 | 9 | 80/60 | 66 | 2 |
| | 9 | 2024/09/05 | DJI M3E | 363 | 8 | 70/50 | 66 | 2 |
| | 10 | 2024/09/05 | DJI M3E | 605 | 10 | 80/60 | 66 | 2 |
| | 11 | 2024/09/06 | DJI M3E | 661 | 11 | 80/60 | 66 | 2 |
| | 12 | 2024/09/06 | DJI M3E | 323 | 13 | 70/50 | 120 | 4 |
| ICE07 | 13 | 2024/09/07 | DJI M3E | 368 | 13 | 70/50 | 96 | 3 |
| | 14 | 2024/09/07 | DJI M2EA | 310 | 12 | 70/50 | 100 | 3 |
| ICE08 | 15 | 2024/09/08 | DJI M3E | 332 | 8 | 70/50 | 66 | 2 |
| | 16 | 2024/09/08 | DJI M2EA | 289 | 12 | 70/50 | 100 | 3 |
| ICE09 | 17 | 2024/09/08 | DJI M3E | 547 | 16 | 80/60 | 96 | 3 |
| | 18 | 2024/09/08 | DJI M2EA | 359 | 15 | 70/50 | 100 | 5 |

Table 1. Parameters for the 18 UAV sea ice observation flight missions.

polar stereographic plane using

$$\begin{aligned} (x_{\text{ref}}, y_{\text{ref}}) &= \text{Proj}(P_{\text{ref}}), \\ (x_{\text{gps}}, y_{\text{gps}}) &= \text{Proj}(P_{\text{gps}}), \\ (x_{\text{img}}, y_{\text{img}}) &= \text{Proj}(P_{\text{img}}). \end{aligned} \tag{1}$$

The sea-ice drift vector is then computed as the displacement between $P_{\text{gps}}$ and $P_{\text{ref}}$:

$$\Delta x = x_{\text{ref}} - x_{\text{gps}}, \quad \Delta y = y_{\text{ref}} - y_{\text{gps}}, \tag{2}$$

which represents the cumulative translational drift of the ice floe relative to the reference frame. This drift vector is applied as a translational correction to the original UAV image position,

$$x_{\text{img}}^{\text{corr}} = x_{\text{img}} + \Delta x, \quad y_{\text{img}}^{\text{corr}} = y_{\text{img}} + \Delta y, \tag{3}$$

thereby shifting the drifting image position back to the fixed reference frame defined by $P_{\text{ref}}$. Finally, the corrected planar coordinates are inversely projected to geographic coordinates,

$$P_{\text{img}}^{\text{corr}}(\text{lat}, \text{lon}) = \text{Proj}^{-1}(x_{\text{img}}^{\text{corr}}, y_{\text{img}}^{\text{corr}}), \tag{4}$$

resulting in the corrected image position. Conceptually, sea ice drift introduces systematic biases in the recorded image positions. The vessel serves as a dynamic base station, with its trajectory used to remove translational drift. Consequently, drift correction transforms UAV imagery into a local coordinate system referenced to vessel GNSS observations, thereby restoring the spatial relationships among the UAV images (Figure 4).

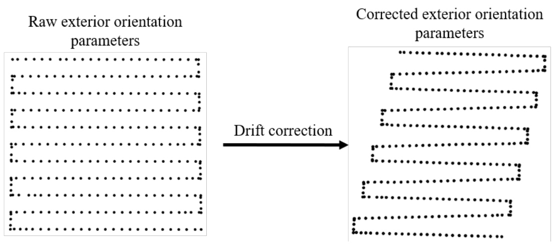


Figure 4. Schematic diagram of the effect of sea ice drift correction on image exterior orientation parameters.

## 2.3 Photogrammetric Processing Workflow

The photogrammetric processing for generating sea ice orthomosaics was conducted in Agisoft Metashape using a standard workflow (aerial triangulation, dense matching, orthorectification, mosaicking). Orthomosaics were generated from the UAV imagery using both the original exterior orientation parameters and those corrected with the drift correction method described in Section 2.2. All 18 missions were processed with identical settings as summarized below (Zhang et al., 2025).

The workspace was defined in WGS 84 / NSIDC Sea Ice Polar Stereographic North (EPSG:3413). Camera accuracy was conservatively set to 100 m/10° to account for Arctic conditions. For each flight, images were imported into a separate chunk. Aerial triangulation used a tie point limit of 5000, with stationary points removed to accommodate weak sea ice textures. Bundle adjustment (BA) was performed incorporating prior camera positions for local referencing (Murtiyoso et al., 2018), followed by camera parameter optimization using the Brown distortion model ($f, c_x, c_y, k_1$–$k_3, p_1, p_2$) with adaptive fitting disabled (Förstner and Wrobel, 2016). Dense image matching was executed using the *High* quality setting. Depth filtering was set to *Mild* to preserve fine sea ice surface details while effectively suppressing noise. To enhance model reliability, dense cloud points with a confidence value $< 3$ were discarded (Nota et al., 2022). Digital elevation models (DEMs) were generated directly from the dense point clouds with interpolation enabled to fill data gaps. Subsequently, orthomosaics were produced at a resolution of 0.05 m using the DEMs as the projection surface, with hole filling enabled.

## 2.4 Sea-Ice Drift Observation and Parameter Acquisition

Ship-borne positioning data recorded the kinematic state of the sea ice. Based on these data, the drift trajectory of the sea ice during the ice station operation period can be mapped, serving as the basis for deriving key kinematic parameters, including drift speed, drift distance, and the relative angle between the drift direction and the flight line (flight-drift angle). Figure 5 illustrates these parameters, plotted over the orthomosaic and the corresponding sea ice drift trajectory. Drift speed is the displacement rate of the icebreaker vessel per unit time, calculated from coordinate differences between consecutive timestamps. Drift distance is the magnitude of total displacement during the observation interval.

The flight-drift angle characterizes the geometric relationship between the drift vector and the UAV flight trajectory. Specifically, the sea ice drift direction is the azimuth of the drift displacement vector, and the UAV flight line direction is the azimuth of the primary flight strip's heading, both measured clockwise from geographic true north. The flight-drift angle is positive when the flight line is clockwise from the drift direction, negative when counter-clockwise, ranging from $[-180°, 180°]$.

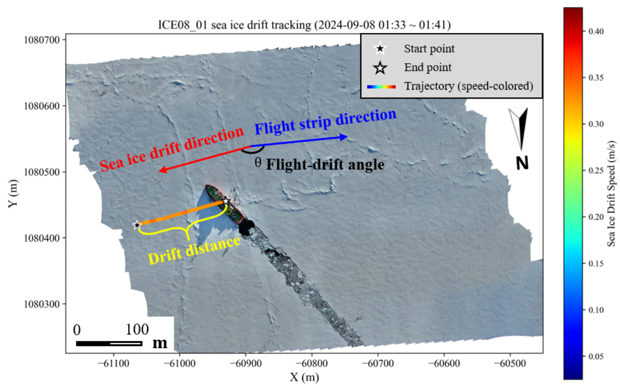


Figure 5. Schematic diagram of sea ice drift parameters.

## 2.5 Relative Accuracy Assessment without GCPs

Since drifting sea-ice scenarios represent a fully dynamic environment, it is impossible to deploy fixed GCPs on the ice, rendering traditional GCP-based accuracy assessment inapplicable (Stott et al., 2020). In this study, relative accuracy of sea ice orthomosaics was evaluated using shipborne reference segments of known length.

As the research vessel was entirely captured in each mission's orthomosaic, several onboard objects or markers of known lengths (e.g., container, A-frame crossbeam) were selected as scale bars for photogrammetric accuracy assessment. Two types of scale bars were defined: constrained scale bars and check scale bars. Constrained scale bars actively participating in BA to optimize camera parameters, while check scale bars strictly reserved for independent accuracy verification. As shown in Figure 6, two constrained and two check scale bars were selected.

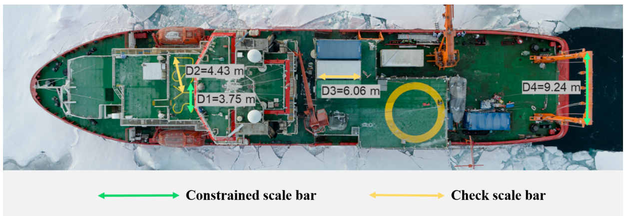


Figure 6. Constrained/check scale bars on board.

The practical implementation was carried out within the Agisoft Metashape. Markers were manually pinned at segment endpoints and designated as either constrained or check scale bars based on the experimental configuration. Notably, check scale bars are always used for accuracy evaluation, while constrained scale bars are only activated in experiments involving scale constraints. The RMSE for check scale bars was computed as:

$$\mathrm{RMSE} = \sqrt{\frac{1}{N}\sum_{i=1}^{N}\left(L_i^{\mathrm{ortho}} - L_i^{\mathrm{ref}}\right)^2}, \tag{5}$$

where $L_i^{\mathrm{ref}}$ is the reference (true) length from field measurements, $L_i^{\mathrm{ortho}}$ is the length measured on the orthomosaic, and $N$ is the number of scale bars used.

### 2.6 Methodology for Analyzing Factors Influencing Orthomosaic Accuracy

Following the relative accuracy assessment, scatter plots and Pearson correlation coefficients were used to examine relationships between check scale bar RMSE and sea ice kinematic parameters. To evaluate the effectiveness of drift correction and scale constraints, comparative analysis was performed under four processing scenarios: (1) no drift correction, no scale constraints (No processing); (2) drift correction applied, no scale constraints (Drift correction only); (3) constrained scale bars activated during BA, no drift correction (Scale constraints only); (4) both drift correction and constrained scale bars applied (Combined two strategies).

## 3. Results

In this section, we present the experimental results from 18 UAV flight missions. The kinematic characteristics of sea ice drift, namely drift speed, drift distance, and flight-drift angle, are derived from shipborne GNSS data. Subsequently, the relative geometric accuracy of the orthomosaics is evaluated under four processing scenarios, followed by regression and correlation analyses to quantify the relationships between accuracy and drift parameters.

### 3.1 UAV-Derived Sea Ice Orthomosaic Results

The orthomosaic results for all individual flights are presented in Figures 10, 11 and 12 in Appendix. Overall, high-quality orthomosaics with good completeness and clear, continuous textures were successfully produced for every flight mission.

### 3.2 Sea Ice Drift Observations Results

The sea ice drift observation results presented in this study consist of the drift trajectories recorded during each flight mission, as well as three key kinematic parameters derived for each mission over its respective flight period: average drift speed, drift distance, and mean flight-drift angle. The full set of trajectories for all 18 flights is provided in Figures 10, 11 and 12 in Appendix. The calculated results for the average drift speed, drift distance, and mean flight line-drift direction angle during each flight mission are recorded in Table 2.

| Flight ID | Drift Speed (m/s) | Drift Distance (m) | Flight-Drift Angle (°) |
|---|---|---|---|
| 1 | 0.08 | 74.14 | 180.70 |
| 2 | 0.04 | 97.66 | 12.06 |
| 3 | 0.13 | 114.81 | -8.40 |
| 4 | 0.25 | 132.62 | -39.09 |
| 5 | 0.24 | 114.99 | 72.23 |
| 6 | 0.14 | 91.86 | -12.08 |
| 7 | 0.30 | 141.03 | -127.18 |
| 8 | 0.26 | 136.18 | 86.26 |
| 9 | 0.11 | 53.70 | -50.68 |
| 10 | 0.06 | 36.07 | 117.28 |
| 11 | 0.14 | 86.59 | 39.71 |
| 12 | 0.08 | 58.86 | 55.33 |
| 13 | 0.29 | 220.24 | -130.47 |
| 14 | 0.28 | 208.22 | 46.45 |
| 15 | 0.33 | 154.18 | -168.23 |
| 16 | 0.33 | 232.03 | 8.53 |
| 17 | 0.12 | 111.52 | 151.99 |
| 18 | 0.13 | 113.40 | 146.73 |

Table 2. Sea ice drift parameters for the 18 flight missions.

As shown in the drift trajectory map, the sea ice drift speed and direction of the 18 flights remained generally stable within each respective operation period. However, when these observations are considered in conjunction with Table 2, distinct differences in drift conditions become apparent among the various flights. The drift speeds across the dataset ranged from 0.04 m/s to 0.33 m/s, and the corresponding drift distances varied from approximately 36 m to 220 m. Furthermore, the angle between the flight trajectory and the drift direction ranged from $-168°$ to $180°$, indicating substantial variation in the relative orientation between flight paths and drift directions among different flights.

### 3.3 Relative Accuracy Assessment Results of Orthomosaics

The relative geometric accuracy of the sea ice orthomosaics for all 18 missions was evaluated by computing the RMSEs of check scale bar lengths within Agisoft Metashape. The assessment results are visually compared in Figure 7.

The accuracy assessment revealed that orthomosaics processed without any correction exhibited considerable variability, with RMSE values ranging from 0.055 m to 0.767 m and a mean of 0.304 m. Applying drift correction alone substantially improves the relative accuracy, reducing the mean RMSE to 0.075 m, with most values distributed between 0.034 m and 0.237 m. When applying only scale constraints, the achieved accuracy ranges from 0.026 m to 0.096 m, with a mean RMSE of 0.043 m. Notably, the combined application of drift correction and scale constraints resulted in a comparable level of accuracy (mean RMSE of 0.043 m), while achieving the highest overall precision, with a minimum error of just 0.018 m.

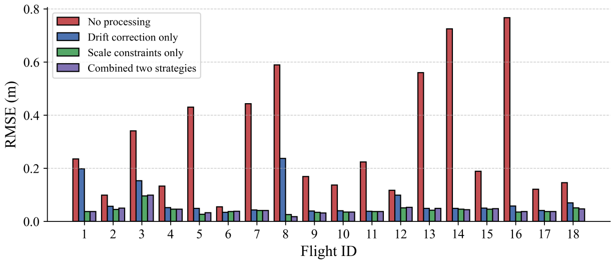


Figure 7. Comparison of RMSE histograms for the 18 flight missions under four processing scenarios.

### 3.4 Relationship Between Accuracy and Sea Ice Drift

To quantify the impact of sea ice drift on orthomosaic fidelity, we performed regression analyses correlating the RMSE of check scale bars with key kinematic parameters across the same four processing schemes as in Section 3.3. Figure 8 presents the scatter plots and regression lines for these scenarios, while the corresponding correlation coefficient matrices are detailed in Figure 9.

Prior to drift correction, regression analysis revealed strong positive correlations between positional error and both drift speed ($r = 0.71$) and drift distance ($r = 0.79$), whereas the flight-drift angle showed negligible influence ($r = -0.13$). This confirms that drift magnitude is the primary driver of geometric error. Conversely, following drift correction or the incorporation of scale constraints, these correlations diminished to near-zero levels. This confirms that both the drift correction and the implementation of constrained scale bars are effective strategies for mitigating the geometric errors induced by sea ice drift.

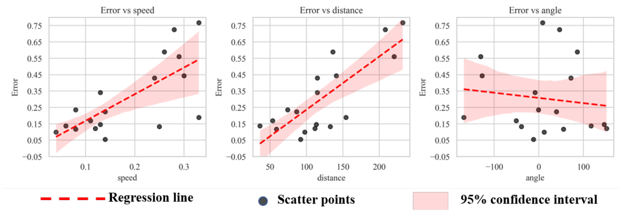


(a) No processing

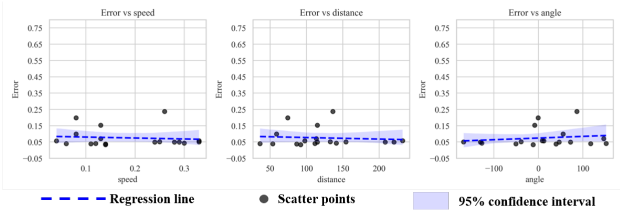


(b) Drift correction only

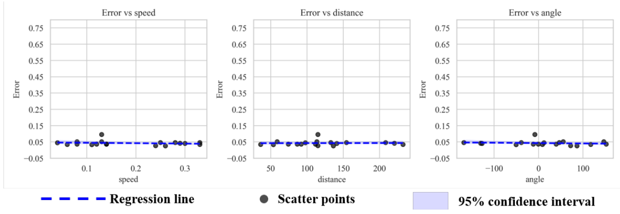


(c) Scale constraints only

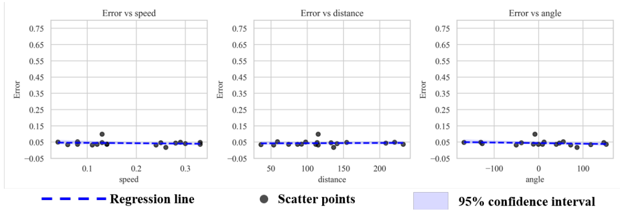


(d) Drift correction and scale constraints

Figure 8. Scatter regression between RMSE and sea ice drift parameters under four processing scenarios.

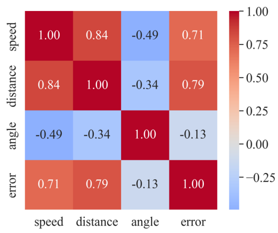


(a) No processing

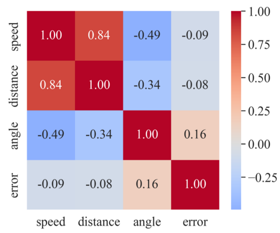


(b) Drift correction only

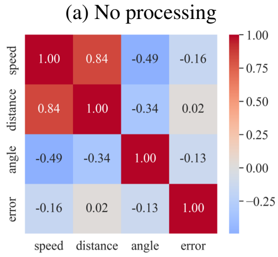


(c) Scale constraints only

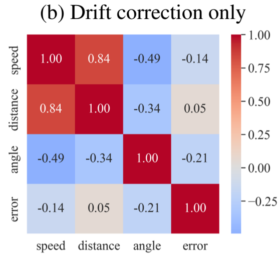


(d) Combined two strategies

Figure 9. Correlation coefficient matrices between RMSE and sea ice drift parameters under four processing scenarios.

## 4. Discussion

### 4.1 Rationale of the Sea Ice Orthomosaic Accuracy Assessment Strategy

Standard photogrammetric accuracy assessment relies on stable, evenly distributed GCPs (Deliry and Avdan, 2021). However, drifting sea ice lacks a fixed reference frame, invalidating the stability assumption required for traditional GCPs. Furthermore, safety and logistical constraints during polar expeditions prevent widespread in-situ measurements across the ice surface (Kim et al., 2021). This study therefore adopts a relative accuracy assessment based on the vessel’s rigid structure. The vessel appears in all flights and maintains stable dimensions, allowing known-length segments to serve as constrained scale bars for optimization and independent check scale bars for validation (Menna et al., 2018). This provides a rigorous and reproducible framework for evaluating scale stability under drifting conditions.

Despite its practicality, this strategy has inherent limitations. Scale bars confined to the vessel may not fully represent errors in distant areas (Roncella and Forlani, 2021), and the method assesses relative scale rather than absolute positioning.

### 4.2 Analysis of Factors Influencing Sea Ice Orthomosaic Accuracy

Figures 8 and 9 indicate that accuracy degradation is primarily driven by the magnitude of geometric inconsistency (drift speed and distance) rather than the flight-drift angle. The latter dictates the spatial pattern of distortion but has a negligible effect on overall RMSE given sufficient overlap (Förstner and Wrobel, 2016). Consequently, drift correction yielded the most pronounced improvements during high-speed drift events (Figure 7), whereas scale constraints consistently enhanced accuracy across all flights independent of drift conditions.

Scene texture also critically influences results. Despite having drift speeds similar to other sorties, Flight 3 exhibited higher RMSE due to extensive open water. The resulting lack of texture compromised feature matching and solution reliability.

## 5. Conclusions

This study established a scale-bar-based framework for assessing UAV photogrammetry accuracy over drifting Arctic sea ice using 18 missions from the FACE2024 expedition, addressing the absence of GCPs via shipborne reference segments. The main findings are summarized as follows.

The proposed optimization strategy achieved substantial improvements in geometric accuracy, reducing the mean RMSE from 0.304 m to 0.043 m, which approaches the GSD level (2–5 cm) despite continuous ice motion. Further analysis revealed that drift magnitude dominates error propagation: drift speed ($r = 0.71$) and drift distance ($r = 0.79$) exhibited strong positive correlations with RMSE, whereas the flight-drift angle showed negligible influence ($r = -0.13$).

In terms of correction effectiveness, drift correction alone reduced the mean RMSE to 0.075 m ($\sim 2 \times$ GSD), achieving improvements of up to 0.6 m under high-drift-speed conditions ($> 0.3$ m/s). Moreover, combining drift correction with scale bar constraints yielded the optimal accuracy of 0.043 m RMSE, demonstrating a clear synergy between kinematic compensation and geometric constraints.

Based on these findings, practical guidance for future Arctic UAV surveys can be summarized as follows: surveys should target scenes with minimal open water and be scheduled during periods of low ice drift speed ($< 0.1$ m/s); additionally, ship-based drift correction should be applied as standard preprocessing, and shipborne rigid features should be employed as scale constraints when GCPs are unavailable.

In summary, with appropriate drift correction and scale bar optimization, commercial UAV platforms and SfM/MVS software can generate orthomosaics with sufficient geometric fidelity for Arctic sea ice research. The methodology is transferable to other dynamic environments (e.g., glaciers and river ice) where GCP-based accuracy assessment is impractical (Florinsky et al., 2020; Wang et al., 2022). Future work will explore integration with multi-source reference data (e.g., InSAR, buoys) (Koo and Rahnemoonfar, 2024; Rabault et al., 2024) to further enhance accuracy and robustness.

## 6. Acknowledgment

This research was jointly supported by the National Natural Science Foundation of China (Grant No. 42506246) and the National Key Technologies Research and Development Program of China (Grant No. 2023YFC2809100). Gratitude ought to be expressed to all members participating in the Following Arctic/Antarctic iCE 2024 (FACE2024) Expedition aboard the RV Zhong Shan Da Xue Ji Di for their valuable field support, both physically and morally.

## References

Chen, F., Antropova, Y., Bonneau, J., Crawford, A. J., Leclair Brideau, B., Sepúlveda Steiner, O., Mueller, D., Park, S., MacAyeal, D. R., 2023. Small-scale, short-term seismic field survey on milne ice shelf. *AGU Fall Meeting Abstracts*, C13C–1134.

Deliry, S. I., Avdan, U., 2021. Accuracy of Unmanned Aerial Systems Photogrammetry and Structure from Motion in Surveying and Mapping: A Review. *Journal of the Indian Society of Remote Sensing*. doi.org/10.1007/s12524-021-01366-x.

Divine, D. V., Pedersen, C. A., Karlsen, T. I., Aas, H. F., Granskog, M. A., Hudson, S. R., Gerland, S., 2016. Photogrammetric Retrieval and Analysis of Small Scale Sea Ice Topography during Summer Melt. *Cold Regions Science and Technology*, 129, 77–84. doi.org/10.1016/j.coldregions.2016.06.006.

Elkhrachy, I., 2021. Accuracy Assessment of Low-Cost Unmanned Aerial Vehicle (UAV) Photogrammetry. *Alexandria Engineering Journal*, 60(6), 5579–5590. doi.org/10.1016/j.aej.2021.04.011.

Florinsky, I., Skrypitsyna, T., Bliakharskii, D., Ishalina, O. T., Kiseleva, A., 2020. Towards the Modeling of Glacier Microtopography Using High-Resolution Data from Unmanned Aerial Survey. *ISPRS - International Archives of the Photogrammetry, Remote Sensing and Spatial Information Sciences*, XLIII-B2-2020, 1065–1071. doi.org/10.5194/isprs-archives-XLIII-B2-2020-1065-2020.

Förstner, W., Wrobel, B. P., 2016. *Photogrammetric computer vision*. 6, Springer.

Kim, J.-I., Hyun, C.-U., Han, H., Kim, H.-C., 2021. Digital Surface Model Generation for Drifting Arctic Sea Ice with Low-Textured Surfaces Based on Drone Images. *ISPRS Journal of Photogrammetry and Remote Sensing*, 172, 147–159. doi.org/10.1016/j.isprsjprs.2020.12.008.

Komarov, A. S., Buehner, M., 2021. Sea ice concentration from the radarsat constellation mission for numerical sea ice prediction. *2021 IEEE 19th International Symposium on Antenna Technology and Applied Electromagnetics (ANTEM)*, 1–2.

Koo, Y., Rahnemoonfar, M., 2024. Hierarchical Information-Sharing Convolutional Neural Network for the Prediction of Arctic Sea Ice Concentration and Velocity. *IEEE Transactions on Geoscience and Remote Sensing*, 62, 1–13. doi.org/10.1109/TGRS.2024.3501094.

Li, Y., Qiao, G., Popov, S., Cui, X., Florinsky, I. V., Yuan, X., Wang, L., 2023. Unmanned Aerial Vehicle Remote Sensing for Antarctic Research: A Review of Progress, Current Applications, and Future Use Cases. *IEEE Geoscience and Remote Sensing Magazine*, 11(1), 73–93. doi.org/10.1109/MGRS.2022.3227056.

Menna, F., Nocerino, E., Drap, P., Remondino, F., Murtiyoso, A., Grussenmeyer, P., Börlin, N., 2018. Improving Underwater Accuracy by Empirical Weighting of Image Observations. *The International Archives of the Photogrammetry, Remote Sensing and Spatial Information Sciences*, XLII-2, 699–705. doi.org/10.5194/isprs-archives-XLII-2-699-2018.

Muilwijk, M., Hattermann, T., Martin, T., Granskog, M. A., 2024. Future Sea Ice Weakening Amplifies Wind-Driven Trends in Surface Stress and Arctic Ocean Spin-Up. *Nature Communications*, 15(1), 6889. doi.org/10.1038/s41467-024-50874-0.

Murtiyoso, A., Grussenmeyer, P., Börlin, N., Vandermeerschen, J., Freville, T., 2018. Open Source and Independent Methods for Bundle Adjustment Assessment in Close-Range UAV Photogrammetry. *Drones*, 2(1), 3. doi.org/10.3390/drones2010003.

Neckel, N., Fuchs, N., Birnbaum, G., Hutter, N., Jutila, A., Buth, L., von Albedyll, L., Ricker, R., Haas, C., 2023. Helicopter-Borne RGB Orthomosaics and Photogrammetric Digital Elevation Models from the MOSAiC Expedition. *Scientific Data*, 10(1), 426. doi.org/10.1038/s41597-023-02318-5.

Nota, E. W., Nijland, W., De Haas, T., 2022. Improving UAV-SfM Time-Series Accuracy by Co-Alignment and Contributions of Ground Control or RTK Positioning. *International Journal of Applied Earth Observation and Geoinformation*, 109, 102772. doi.org/10.1016/j.jag.2022.102772.

Rabault, J., Taelman, C., Idžanović, M., Hope, G., Nose, T., Kristoffersen, Y., Jensen, A., Breivik, Ø., Bryhni, H. T., Hoppmann, M., Demchev, D., Korosov, A., Johansson, M., Eltoft, T., Dagestad, K.-F., Röhrs, J., Eriksson, L., Moro, M. D., Rikardsen, E. S. U., Waseda, T., Kodaira, T., Lohse, J., Desjonquères, T., Olsen, S., Gundersen, O., de Aguiar, V. C. M., Karlsen, T., Babanin, A., Voermans, J., Park, J.-W., Müller, M., 2024. A Position and Wave Spectra Dataset of Marginal Ice Zone Dynamics Collected around Svalbard in 2022 and 2023. *Scientific Data*, 11(1), 1417. doi.org/10.1038/s41597-024-04281-1.

Rack, W., Price, D., Haas, C., Langhorne, P. J., Leonard, G. H., 2021. Sea Ice Thickness in the Western Ross Sea. *Geophysical Research Letters*, 48(1), e2020GL090866. doi.org/10.1029/2020GL090866.

Roncella, R., Forlani, G., 2021. UAV Block Geometry Design and Camera Calibration: A Simulation Study. *Sensors*, 21(18), 6090. doi.org/10.3390/s21186090.

Stott, E., Williams, R. D., Hoey, T. B., 2020. Ground Control Point Distribution for Accurate Kilometre-Scale Topographic Mapping Using an RTK-GNSS Unmanned Aerial Vehicle and SfM Photogrammetry. *Drones*, 4(3), 55. doi.org/10.3390/drones4030055.

Wang, E., Hu, S., Han, H., Li, Y., Ren, Z., Du, S., 2022. Ice Velocity in Upstream of Heilongjiang Based on UAV Low-Altitude Remote Sensing and the SIFT Algorithm. *Water*, 14(12), 1957. doi.org/10.3390/w14121957.

Zhang, S., Zheng, L., Zhou, H., Zhao, Q., Li, J., Xia, Y., Zhang, W., Cheng, X., 2025. Fine-Scale Antarctic Grounded Ice Cliff 3D Calving Monitoring Based on Multi-Temporal UAV Photogrammetry without Ground Control. *International Journal of Applied Earth Observation and Geoinformation*, 142, 104620. doi.org/10.1016/j.jag.2025.104620.

## Appendix

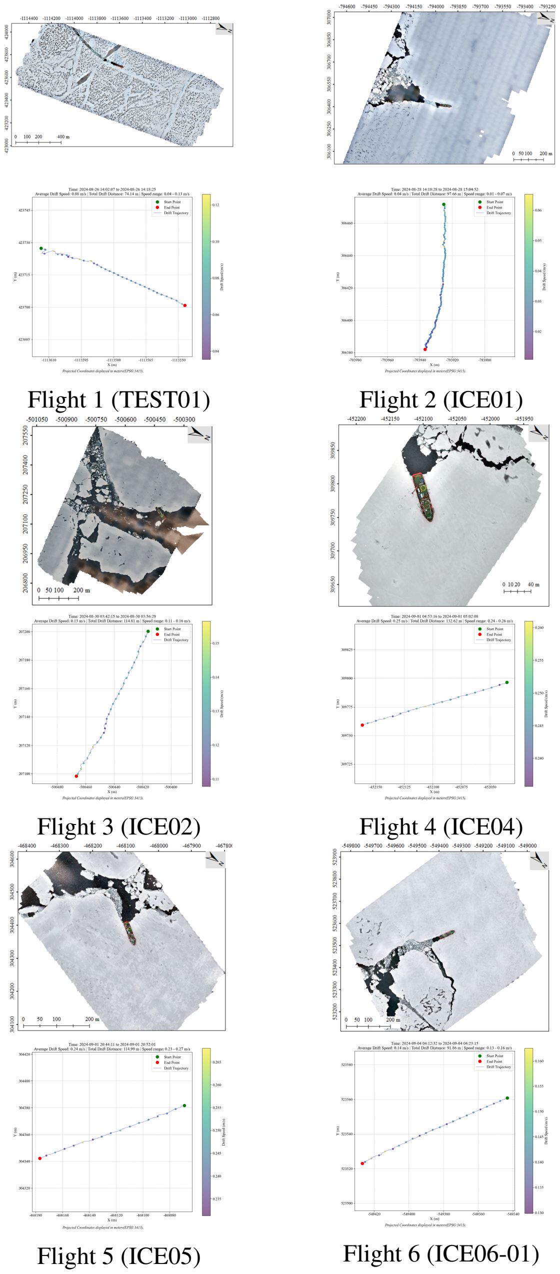


Figure 10. Orthomosaic results (top) and drift trajectories (bottom) for Flights 1-6.

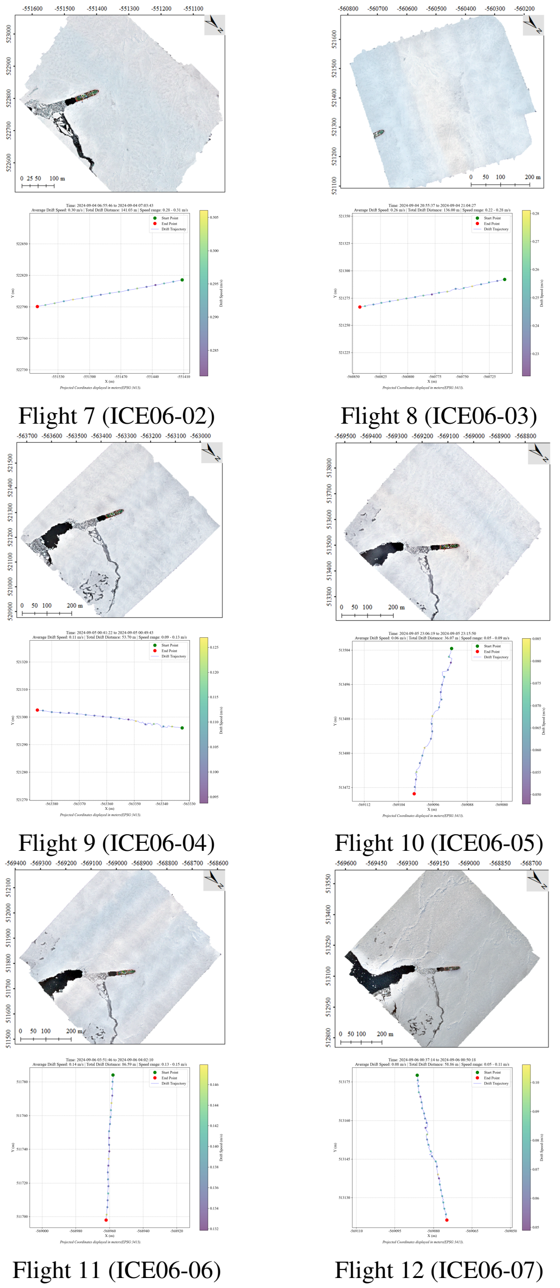


Figure 11. Orthomosaic results (top) and drift trajectories (bottom) for Flights 7-12.

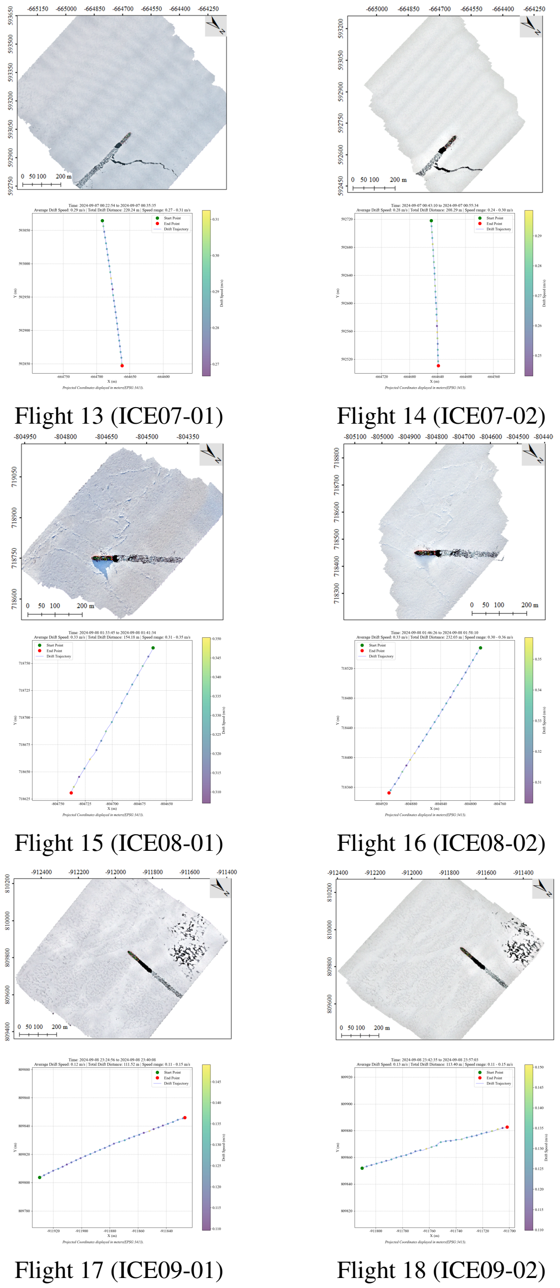


Figure 12. Orthomosaic results (top) and drift trajectories (bottom) for Flights 13-18.